

Anisotropic emission of direct photons and thermal dileptons from Au+Au collisions at $\sqrt{s_{NN}} = 200$ GeV with EPOS3

Sheng-Xu Liu,¹ Fu-Ming Liu^{*,1} Klaus Werner,² and Meng Yue¹

¹*Key laboratory of Quark and Lepton Physics (Ministry of Education),
Central China Normal University, Wuhan, China*

²*Laboratoire SUBATECH, University of Nantes - IN2P3/CNRS - Ecole desMines, Nantes, France*
(Dated: July 12, 2016)

Electromagnetic probes such as direct photons and dileptons are crucial to study the properties of a Quark-Gluon Plasma (QGP) created in heavy ion collisions. Based on the (3+1)-dimensional event-by-event viscous hydrodynamic model EPOS 3.102, we calculated the anisotropic emission of thermal photons and dileptons in Au+Au collisions at the Relativistic Heavy Ion Collider (RHIC) energy $\sqrt{s_{NN}} = 200$ GeV. Thermal emissions from both QGP phase and hadronic gas phase are considered, with AMY rate for photons and Lattice QCD based rates for dileptons in QGP phase. For emission from hadron gas phase, rates based vector meson dominant model are used for both photons and dileptons. Non-thermal contribution to direct photons is calculated with next to leading order QCD. STAR cocktail data are directly used for non-thermal contribution to dileptons. With the same space-time evolution of the collision systems, the two penetrating probes, photons and dileptons show some consistency, ie, the emission of both thermal photons and dileptons are underestimated, compared with the transverse momentum spectra of direct photons measured by PHENIX collaboration and the invariant mass spectra of dileptons measured by STAR collaboration, for all centrality classes. With a good constraint of anisotropy of the plasma via the elliptic flow and triangular flow of charged hadrons, the resulted elliptic flow and triangular flow of direct photons agree with PHENIX measurements reasonably well. Thus we made predictions to the flows of thermal dileptons. The elliptic flow of thermal dileptons is predicted larger than the available results from other models, and comparable to the STAR measurement referring to all dileptons (thermal + cocktail) for minimal bias collisions.

PACS numbers:

I. INTRODUCTION

Electro-magnetic probes such as direct photons and dileptons are considered as golden probes to a quark-gluon plasma (QGP) [1]. Because of the small electro-magnetic coupling, they are expected to penetrate the hot dense matter created in relativistic heavy ion collisions and to carry us the information of the hot dense matter. The observed large elliptic flow of direct photons was once a puzzle in relativistic heavy ion physics [2]. Our previous work provided a possibility to this puzzle with the delayed QGP formation in relativistic heavy ion collisions [4], reveals that direct photons, different from bulk hadrons, are able to carry the information of the system at the very early stage. Recently the McGill group made a nice reproduction of the elliptic flow, with a detailed investigation of the effects from viscosity [5].

In this work, we will investigate the transverse momentum spectra, elliptic flow v_2 and triangular flow v_3 of direct photons from Au+Au collisions at the Relativistic Heavy Ion Collider (RHIC) energy $\sqrt{s_{NN}} = 200$ GeV, without any additional parameter to EPOS3, a hydrodynamic model which reasonably reproduces hadronic data such as rapidity distributions, transverse momenta, el-

liptic flows and triangular flows in this collision systems. The comparison to the measured direct photon data will be performed thereafter.

Then based on the same description of the space-time evolution of the collision systems, we will investigate the anisotropic emission of thermal dileptons. In addition to the thermal sources, dileptons may also be produced from non-thermal sources such as primordial Drell-Yan annihilation and electromagnetic final-state decays of long-lived hadrons. To account for these, STAR cocktail results from Refs [6] have been employed in this paper. The calculated invariant mass spectrum will be compared to the data measured by the STAR Collaboration [6]. Then we will check the elliptic flow v_2 and high order coefficient v_n of the thermal dielectrons from different

The paper is organized as following. In section 2, we will introduce our calculation approach of direct photons and thermal dileptons, such as the space-time evolution of the collision system based on hydrodynamic model EPOS3, and thermal dilepton emission rates from QGP phase and hadronic phase. In section 3 we will present the results, first the relevant hadronic results such as elliptic flow v_2 and triangular flow v_3 , then systematically the results of photons and dileptons. Finally, discussion and conclusion in section 4.

*Corresponding author: liufm@mail.ccnu.edu.cn

II. CALCULATION APPROACH

Both thermal photons and thermal dileptons are calculated as the integral of the emission rates over the space-time evolution of the collision systems. So we first introduce the space-time evolution of the collision systems. Then we introduce the integral formula and the rates.

A. The space-time evolution of the collision system with EPOS3

As explained in [7], EPOS3 is an event generator based on a 3+1D viscous hydrodynamic evolution starting from flux tube initial conditions, which are generated in the Gribov-Regge multiple scattering framework [8]. An individual scattering is referred to as Pomeron, identified with a parton ladder, eventually showing up as flux tubes (or strings). Each parton ladder is composed of a pQCD hard process, plus initial and final state linear parton emission. Nonlinear effects are considered by using saturation scales Q_s , depending on the energy and the number of participants connected to the Pomeron in question.

The final state partonic system (corresponding to a Pomeron) amounts to (usually two) color flux tubes, being mainly longitudinal, with transversely moving pieces carrying the p_t of the partons from hard scatterings [8, 9]. One has two flux tubes, based on the cylindrical topology of the Pomerons, but each quark-antiquark pair in the parton ladder will cut a string into two, in this sense one may have more than two flux tubes. In any case, these flux tubes constitute eventually both bulk matter, also referred to as “core” [10] (which thermalizes, flows, and finally hadronizes) and jets (also referred to as “corona”), according to some criteria based on the energy of the string segments and the local string density.

Concerning the core, we use a 3+1D viscous hydrodynamic approach, employing a realistic equation of state, compatible with lQCD results. We employ for all calculations in this paper a value of $\eta/S = 0.08$. Whenever a temperature of $T_H = 168$ MeV is reached, the usual Cooper-Frye procedure is used to convert the fluid into particles. From this point on, a hadronic cascade [11], based on hadronic cross sections is employed.

So we have two phases. In QGP phase, the hydrodynamical expansion can naturally provide us the complete space-time information, i.e. the four fluid velocity u^μ and temperature T at any given space-time x , starting from some initial proper time τ_0 . In the hadronic phase, we have from EPOS a complete description of hadron trajectories. We use this to compute energy densities, flow velocities and net baryon density. Assuming that the system may be approximated by a resonance gas in equilibrium, we use the corresponding equation of state, c.f. Appendix C of [9], to get the space-time information, such as the four fluid velocity u^μ and temperature T at any given space-time x .

In the following are shown some basic results of the

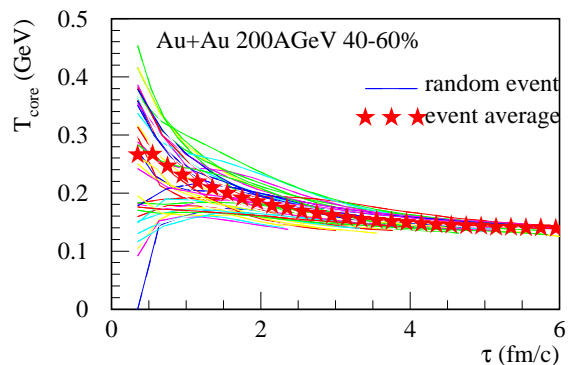


Figure 1: (Color Online) The time evolution of the temperature at the center point $(x,y,z)=(0,0,0)$ in AuAu collisions at $\sqrt{s_{NN}} = 200$ GeV with centrality 40-60%. Thin lines stand for random events. Stars for event averaged results.

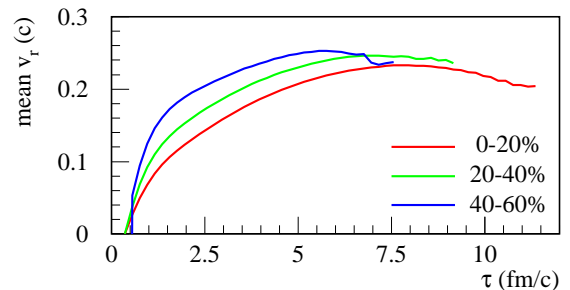


Figure 2: (Color Online) The time evolution of mean radial flow velocity in AuAu collisions at $\sqrt{s_{NN}} = 200$ GeV for three centrality classes, 0-20%, 20-40% and 40-60%.

space-time evolution for AuAu collisions at RHIC energy $\sqrt{s_{NN}} = 200$ GeV.

First is shown the time evolution of the temperature at the center point $(x,y,z)=(0,0,0)$ of the created hot dense matter in AuAu collisions at $\sqrt{s_{NN}} = 200$ GeV with centrality 40-60% in Fig. 1. Here the thin lines are results of some random EPOS3 events, stars for the averaged result over many events. In most events, the center temperature decreases with time. So does the event-averaged result. However, the core temperature fluctuates from event to event quite a lot. In some events, the core temperature may increase during some short time range, being heated by the domain nearby.

Second in Fig. 2 is shown the time evolution of the mean radial velocity in the Au+Au systems at $\sqrt{s_{NN}} = 200$ GeV for three centrality classes, 0-20%, 20-40% and 40-60%. Radial flow $v_r = \sqrt{v_x^2 + v_y^2}$ has some effect to the transverse momentum spectrum of produced particles. Moreover, it generates elliptic flow v_2 , with its strength and asymmetry along azimuthal direction. Here is shown only the averaged strength at each given time τ , the energy density weighted result over the whole space, then event average. We can see the flow velocity is initially zero. Then it increases rapidly at the beginning

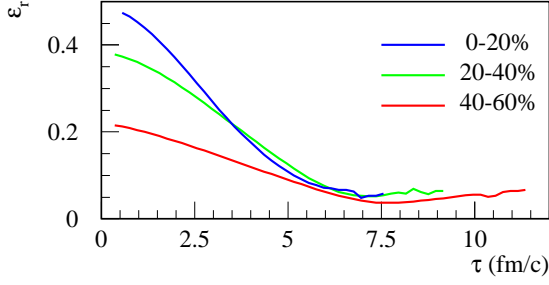


Figure 3: (Color Online) The time evolution of the space eccentricity in AuAu collisions at $\sqrt{s_{NN}} = 200$ GeV for three centrality classes, 0-20%, 20-40% and 40-60%.

then slowly saturates. The system of more central collisions has a longer life, but the upper limit of the mean radial velocity depends very weakly on centrality.

Finally in Fig. 3 is shown the time evolution of the space eccentricity in AuAu collisions at $\sqrt{s_{NN}} = 200$ GeV for three centrality classes, 0-20%, 20-40% and 40-60%. The space eccentricity is calculated as

$$\epsilon_r = \frac{\langle y^2 - x^2 \rangle}{\langle y^2 + x^2 \rangle}, \quad (1)$$

Here $\langle \dots \rangle$ stands for an energy density weighted space integral, additionally event average is also made. We can see the collision system initially carries a large eccentricity on average, because of the overlapping shape of the colliding nuclei. With the hydrodynamic expansion, the space eccentricity decreases.

B. Transverse momentum of direct photons and Invariant mass spectrum of dileptons

The transverse momentum spectra of thermal photons can be written as

$$\frac{dN}{dy d^2p_t} = \int d^4x \Gamma(E^*, T) \quad (2)$$

where $\Gamma(E^*, T)$ is the Lorentz invariant thermal photons emission rate which covers the contributions from the QGP phase [12] and HG phase [13] as our previous work, $d^4x = \tau d\tau dx dy d\eta$ being the volume-element, and the photon energy in the local rest frame

$$E^* = p^\mu u_\mu = \gamma p_0 - \gamma \vec{p} \cdot \vec{v} \quad (3)$$

with $p^\mu = (E, \vec{p})$ is the photon's four momentum in the laboratory frame, $u^\mu = (\gamma, \vec{v})$ is the four flow velocity, $v^2 = \vec{v} \cdot \vec{v}$ and $\gamma = 1/\sqrt{1-v^2/c^2}$. Temperature T and the fluid velocity $u^\mu = (\gamma, \vec{v})$ is provided by EPOS3 as explained above. The space-time integral starts from the default initial time of EPOS3, $\tau_0 = 0.35$ fm/c, until the end of the system evolution shown on average in Fig. 2.

The invariant mass spectrum of thermal dileptons reads

$$\frac{dN}{dM}(M) = \int d^4x \frac{M d^3q}{q_0} \Gamma'(T, q^*) \quad (4)$$

where M and q are the invariant mass and four momentum of the dilepton pair in the laboratory frame, satisfying $M^2 = q^2$. Again, the fluid velocity $u^\mu = (\gamma, \vec{v})$ connects the four-momentum of the dilepton q and q^* , in the laboratory frame and the local rest frame of the hot dense matter, respectively, via

$$q_0^* = \gamma q_0 - \gamma \vec{q} \cdot \vec{v} \quad (5)$$

and

$$\vec{q}^* = \vec{q} + (\gamma - 1)(\vec{q} \cdot \vec{v}) \cdot \vec{v}/v^2 - \gamma q^0 \vec{v}. \quad (6)$$

The Lorentz invariant dilepton emission rates

$$\Gamma'(T, q^*) = \frac{dR}{d^4q}(T, q^*) = \frac{dN}{d^4x d^4q}(T, q^*) \quad (7)$$

will be explained in detail in the following, since this is our first dilepton paper. The momentum integral ranges from 0 to 5 GeV/c (results do not depend on the upper bound as long as it is much bigger than the temperature). The STAR data are obtained with cuts on the single-electron tracks in the lab, like $p_t > 0.2$ GeV/c and $|\eta| < 0.9$. These have a significant impact on both yields and shape of the low-mass dilepton spectrum. We simulate virtual photon with a given four-momentum decay into electron-positron pair, then obtain the acceptance efficiency of a virtual photon according to the η and p_t distribution of produced electrons. Then put this acceptance factor into the space-time integral.

There are also non-thermal sources for direct photons and dileptons. Non-thermal sources to dileptons such as primordial Drell-Yan annihilation and electromagnetic final-state decays of long-lived hadrons are not calculated. Instead, STAR cocktail results from Refs [6] have been employed. The non-thermal direct photon source is simplified as prompt photons, as a next to leading order QCD calculation in pp collisions [15]. Here we present the p_t spectrum of prompt photons (red solid line) from pp collisions at $\sqrt{s} = 200$ GeV compared with PHENIX data [14, 32] (dots) in 4. A good coincidence in the hard region has been obtained. In heavy ion collisions, nuclear parton distribution functions (nPDF) $G_{a/A}(x)$ is used. For a nucleus with mass A , neutron number N , and proton number Z ,

$$G_{a/A}(x) = \left[\frac{N}{A} G_{a/N}(x) + \frac{Z}{A} G_{a/P}(x) \right] R_a(x, A). \quad (8)$$

where $G_{a/p}(x)$ is PDF in proton, R_a factor is taken into account of shadowing effect and EMC effect [16].

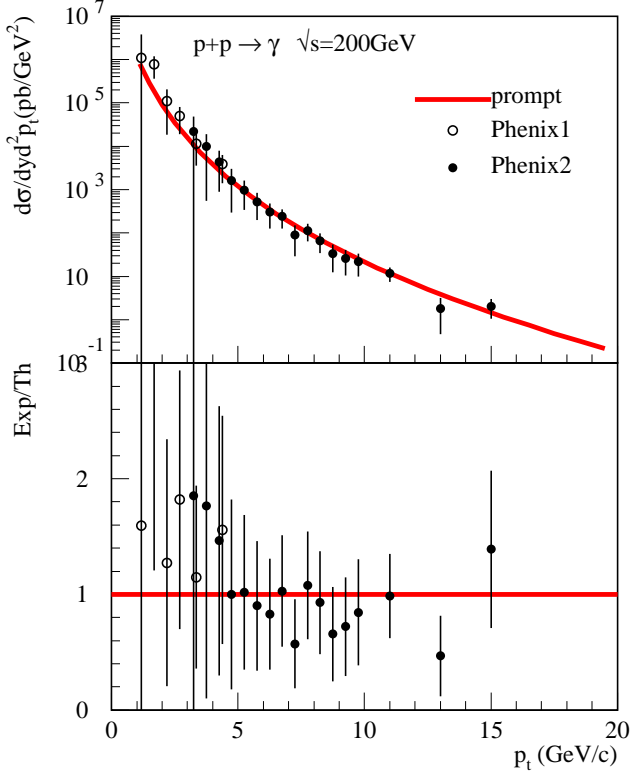


Figure 4: (Color Online) Photon production from pp collisions at $\sqrt{s} = 200$ GeV. The solid line is our next to leading order QCD calculation for prompt photons. Dots are PHENIX data, full [14] and empty [32].

C. Dilepton Emission Rates

This is our first work on dilepton. So it is necessary to explain thermal dilepton emission rates in QGP phase and HG phase in detail. Photon emission rates have been employed in our previous work and kept. For dileptons emitted from the QGP phase, asymptotic freedom implies that the production rate in the intermediate invariant mass region ($1. < M < 3.0 \text{ GeV}/c^2$) at high temperatures and densities can be described by perturbation theory as in Ref.[17]. Recent progress using thermal lattice QCD (lQCD) to calculate dilepton rates nonperturbatively at vanishing three-momentum $q = 0$ has been reported in Ref. [18]. For practical applications, an extrapolation to finite q values is needed. A construction proposed in Ref. [19] and employed in our calculation reads

$$\frac{d^4 R}{d^4 q} = \frac{\alpha^2}{4\pi^4} f^B(q_0, T) C_{\text{EM}} \left\{ 1 + \frac{2T}{q} \ln \left[\frac{1+x_+}{1+x_-} \right] + 2\pi\alpha_s \frac{T^2}{M^2} K F(M^2) \ln \left(1 + \frac{2.912q_0}{4\pi\alpha_s T} \frac{2q_0^2 + M^2}{3q_0^2} \right) \right\}, \quad (9)$$

where α is the electromagnetic coupling constant, $f^B(q_0, T)$ the thermal Bose distribution, $C_{\text{EM}} \equiv$

$\sum_{q=u,d,s} e_q^2$, $x_{\pm} = \exp[-(q_0 \pm q)/2T]$. The quantity α_s is the temperature-dependent strong coupling constant, K a constant factor (equal 2), and finally we have a form factor $F(M^2) = \frac{\Lambda^2}{\Lambda^2 + M^2}$ with $\Lambda = 2T$.

Dilepton emission Rate from hadronic gas is considered with the vector meson dominance model [20], where the hadronic electromagnetic current operator is equal to the linear combination of the known neutral vector meson field operators, most notably $V = \rho, \omega, \phi$. This describes dilepton production successfully [17], where the dilepton emission rate via the vector meson V is [21]

$$\frac{d^4 R_V}{d^4 q} = -\frac{\alpha^2 m_V^4}{\pi^3 M^2 g_V^2} \text{Im} D_V \frac{1}{e^{\frac{q_0}{T}} - 1}, \quad (10)$$

with the coupling constant g_V determined by the measured decay rate of vector-meson to dilepton production in vacuum, and m_V being the mass of the vector-meson. The imaginary part of the retarded vector meson propagator is given as

$$\text{Im} D_V = \frac{\text{Im} \Pi_V}{(M^2 - m_V^2 - \text{Re} \Pi_V)^2 + (\text{Im} \Pi_V)^2}, \quad (11)$$

where Π_V is the self-energy of the vector meson V .

We consider $V = \rho$ and neglect the complexity of ω and ϕ , which seems consistent with the STAR dilepton data taking[6]. The ρ meson self-energy

$$\Pi_\rho = \Pi_\rho^{\text{vac}} + \sum_a \Pi_{\rho a}, \quad (12)$$

for the contribution from the vacuum and from ρ meson scattering with hadrons of type a in the hadronic gas, respectively.

The vacuum part Π_ρ^{vac} is obtained from Gounaris-Sakurai formula as Refs [20, 22], which could describe the pion electromagnetic form factor well, as measured in e^+e^- annihilation Refs [23]:

$$\text{Re} \Pi_\rho^{\text{vac}} = \frac{g_\rho^2 M^2}{48\pi^2} \left[\left(1 - \frac{4m_\pi^2}{M^2} \right)^{\frac{3}{2}} \ln \left| \frac{1 + \sqrt{1 - \frac{4m_\pi^2}{M^2}}}{1 - \sqrt{1 - \frac{4m_\pi^2}{M^2}}} \right| + 8m_\pi^2 \left(\frac{1}{M^2} - \frac{1}{m_\rho^2} \right) - 2 \left(\frac{p_0}{\omega_0} \right)^3 \ln \left(\frac{\omega_0 + p_0}{m_\pi} \right) \right], \quad (13)$$

$$\text{Im} \Pi_\rho^{\text{vac}} = -\frac{g_\rho^2 M^2}{48\pi} \left(1 - \frac{4m_\pi^2}{M^2} \right)^{\frac{3}{2}}. \quad (14)$$

Here, $2\omega_0 = m_\rho = 2\sqrt{m_\pi^2 + p_0^2}$. The vacuum width is $\Gamma_\rho^{\text{vac}} = \frac{g_\rho^2}{48\pi} m_\rho \left(\frac{p_0}{\omega_0} \right)^3$.

The interactive part $\Pi_{\rho a}(E, p)$ is obtained from ρ scattering from hadron of type a in the hadronic gas

$$\Pi_{\rho a}(E, p) = -4\pi \int \frac{d^3 k}{(2\pi)^3} n_a(\omega) \frac{\sqrt{s}}{\omega} f_{\rho a}^{c.m.}(s), \quad (15)$$

where $f^{c.m.}$ is the forward scattering amplitude in the c.m. system, E and p are the energy and momentum of

the ρ meson, $\omega^2 = m_a^2 + k^2$. The most copious hadrons in the hadronic gas such as π mesons ($a = \pi$) and nucleons ($a = N$) are considered in our calculation. The quantity n_a is the Bose-Einstein occupation number of π mesons and the Fermi-Dirac occupation number for nucleons, with temperature T and baryon chemical potential μ_B of the thermal bath provided by EPOS3 mentioned above. According to Eq.(5-6), the emitted dileptons will get a Lorentz boost with the collective flow velocity offered by EPOS3, so the interactive term of self-energy and the resulted emission rate are calculated in the rest frame of the thermal bath.

The ρa forward scattering amplitude in the center-of-mass frame could be written as

$$f_{\rho a}^{c.m.} = (1-x)f_{\text{Res}} + xf_{\text{Reg}} + f_{\text{Pom}}, \quad (16)$$

where the Pomeron term is dual to the background upon which the resonances are superimposed, x is a function that matches the low energy Breit-Wigner resonances and high energy Reggions (dual to s-channel resonances) smoothly:

$$x = 0.5(1 + \tanh(\frac{E_\rho - m_\rho - E_\Delta}{0.3})), \quad (17)$$

where E_Δ is 1GeV and 4GeV for $\rho\pi$ and ρN scattering, respectively[24].

Regge and Pomeron term have the same form [25]:

$$f_{\text{Reg/Pom}} = -\frac{q_{c.m.}}{4\pi s} \frac{1 + e^{-i\pi\alpha}}{\sin \pi\alpha} s^\alpha r^{\rho a}, \quad (18)$$

where the intercept α and residue $r^{\rho N}$, $r^{\rho\pi}$ are 0.642, 28.59, 12.74 for Regges and 1.093, 11.88, 7.508 for Pomerons, respectively (the units yield a cross section in mb with energy in GeV).

The resonance term is [25]:

$$f_{\text{Res}} = \frac{1}{2q_{c.m.}} \sum_R W_{\rho a}^R \frac{\Gamma_{R \rightarrow \rho a}}{M_R - \sqrt{s} - \frac{i}{2}\Gamma_R}, \quad (19)$$

which involves a sum over a series of Breit-Wigner resonances of mass M_R and total width Γ_R . The resonances R used in our calculation are listed in table I for $a = \pi$ and table II for $a = N$, with R 's name, mass, decay width, branching ratio, spin, isospin and relative angular momentum Ref. [24, 25].

Table I: Meson resonances R for $\rho\pi$ processes.

Name(R)	Mass(M_R)	Γ	BR	S	IS	L
$\phi(1020)$	1.020	0.0045	0.13	1	0	1
$h_1(1170)$	1.170	0.36	1	1	0	0
$a_1(1260)$	1.230	0.40	0.68	1	1	0
$\pi(1300)$	1.300	0.40	0.32	0	1	1
$a_2(1320)$	1.318	0.107	0.70	2	1	2
$\omega(1420)$	1.419	0.174	1	1	0	1

The c.m. amplitude $f_{\rho a}^{c.m.}$ and the scattering amplitude in the rest frame of a , $f_{\rho a}$, are related by

$$\sqrt{s} f_{\rho a}^{c.m.}(s) = m_a f_{\rho a}(E_\rho), \quad (20)$$

with $s = m_\rho^2 + m_a^2 + 2E_\rho m_a$. The latter is plotted in Fig.5 and Fig.6, for $\rho\pi$ and ρN scattering, respectively. The total contribution (Resonances + Pomeron background + Regge) in both are shown as black solid lines, and both are consistent with Ref. [25]. Each individual process $\rho\pi \rightarrow R$ is also shown in Fig.5. Their sum is shown as black dashed line. We can see that the contribution of resonances dominates the low energy scattering, and the dominant channels are $R = a_1(1260)$ and $h_1(1170)$ due to their large branch ratios. In Fig.6, the relevant individual channels $\rho N \rightarrow R$ are shown. The black dashed line is the total baryon resonances contribution, among which $R = \Delta(1905)$, $N(2000)$ and $N(1720)$ dominate both the imaginary and the real part of the the amplitude for ρN scattering.

Putting the forward scattering amplitudes together, we get the interactive term of self-energy of ρ -meson. The imaginary and real parts are shown in Fig.7, for a fixed ρ -meson three-momentum $q = 0.3$ GeV/c at $T = 150$ MeV, with $\rho\pi$ scattering dotted lines and ρN scattering dashed-dotted lines, respectively. The contribution from vacuum is plotted as dashed lines. The total one is plotted as solid lines. The vacuum contributes when $M > 2m_\pi$, then dominates over a wide region. To illustrate the q -dependence, the total contribution with $q = 1$ GeV/c is also presented. Because of rho-pi scattering rather than rho-N scattering, the imaginary part of the self-energy has an evident q -dependence at the low invariant mass.

Yet, the interaction with the medium gives a broadening effect to the spectral density, $\rho(q) = -\text{Im}D_\rho(q)/\pi$. In Fig.8, $\text{Im}D_\rho$ is plotted as a function of invariant mass M

Table II: Baryon resonances R for ρN processes.

Name(R)	Mass(M_R)	Γ	BR	S	IS	L
N(2090)	1.928	0.414	0.49	0.5	0.5	0
N(1700)	1.737	0.249	0.13	1.5	0.5	0
N(2080)	1.804	0.447	0.26	1.5	0.5	0
N(2190)	2.127	0.547	0.29	3.5	0.5	2
N(2100)	1.885	0.113	0.27	0.5	0.5	1
N(1720)	1.717	0.383	0.87	1.5	0.5	1
N(1900)	1.879	0.498	0.44	1.5	0.5	1
N(2000)	1.903	0.494	0.60	2.5	0.5	1
$\Delta(1900)$	1.920	0.263	0.38	0.5	1.5	0
$\Delta(1700)$	1.762	0.599	0.08	1.5	1.5	0
$\Delta(1940)$	2.057	0.460	0.35	1.5	1.5	0
$\Delta(2000)$	1.752	0.251	0.22	2.5	1.5	1
$\Delta(1905)$	1.881	0.327	0.86	2.5	1.5	1
N(1520)	1.520	0.124	0.008	1.5	0.5	0
$\Delta(1232)$	1.232	0.118	0.006	1.5	1.5	1

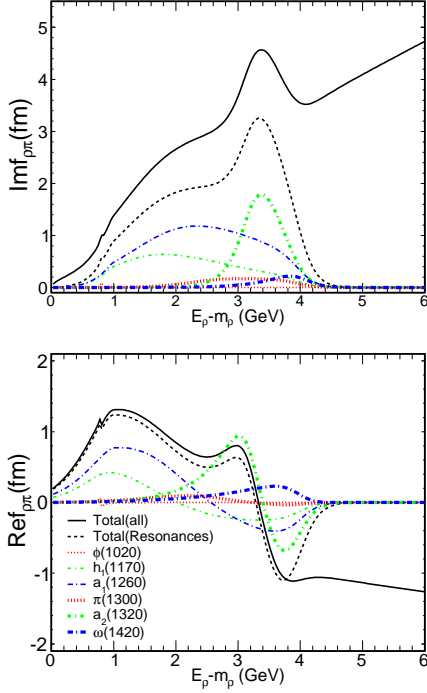


Figure 5: (Color Online) The individual and total amplitude for $\rho\pi \rightarrow R$ scattering (imaginary part: upper panel, real part: lower panel).

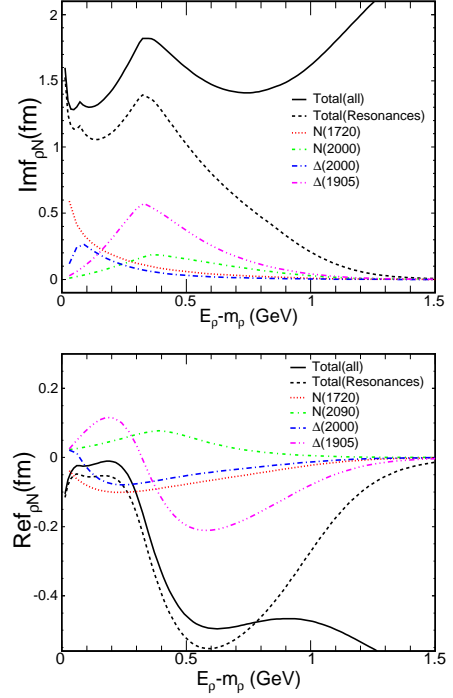


Figure 6: (Color Online) The relevant individual and total amplitude for $\rho N \rightarrow R$ scattering (imaginary part: upper panel, real part: lower panel).

for a ρ -meson momentum of $q = 0.3$ GeV/c, in a thermal hadronic gas of temperature $T=100, 150$ and 200 MeV, respectively. The vacuum contribution by itself is plotted as a red solid line. With the increase of medium temperature, the ρ -meson scattering with hadron a in the medium broadens the spectral density more and more, but the peak remains close to ρ -meson mass. (Note: $T=200$ MeV is only to visualize the broadening effect, though it is too high for hadronic gas.)

The emission rates at different phases are now obtained via Eq.(9-10). In Fig.9, the emission rate from the QGP phase is plotted as red thin lines (dotted: 200 MeV, solid: 150 MeV), from the HG phase as green thick lines (dotted: 150 MeV, solid: 100 MeV). A higher temperature makes a stronger di-electron emission. Nevertheless the HG phase provides a pronounced peak around the ρ -meson mass 775 MeV which exceeds the QGP contribution. This peak is essentially due to the vacuum term in the self-energy (black dashed line). The emission rate from HG phase at 150 MeV obtained from effective interaction Lagrangians [26] is also shown as a blue dotted dashed line. It is interesting to see the two rates are quite close to each other, though different approaches and channels are considered.

We should mention here that the above-mentioned emission rates work typically for ideal hydrodynamics. For viscous hydrodynamics such as EPOS3, a viscous correction is needed. The effect of shear viscosity to the

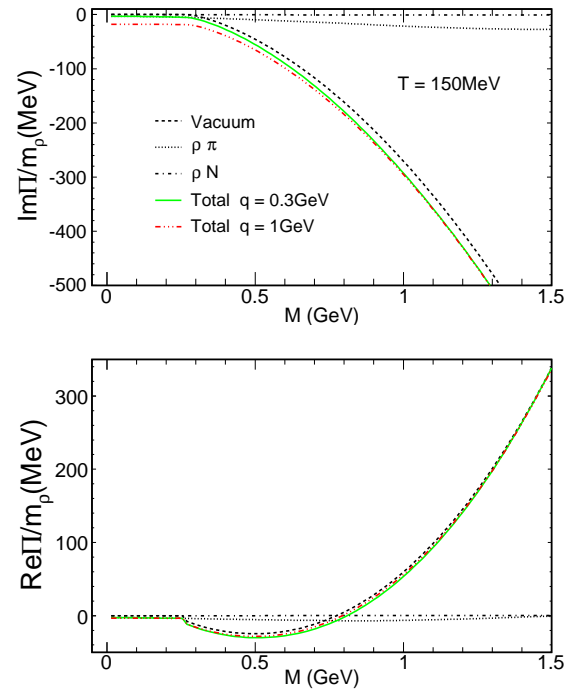


Figure 7: The self-energy of ρ -meson.

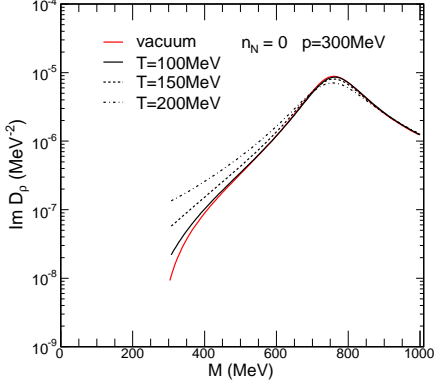


Figure 8: (Color Online) The imaginary part of the ρ meson propagators as a function of invariant mass for a momentum of $300 \text{ MeV}/c$ and a nucleon density of $n_N = 0$. Results are shown for vacuum (red solid line) and three temperatures, $T = 100 \text{ MeV}/c$ (black solid line), $T = 150 \text{ MeV}/c$ (black dashed line), $T = 200 \text{ MeV}/c$ (black dashed-dotted line).

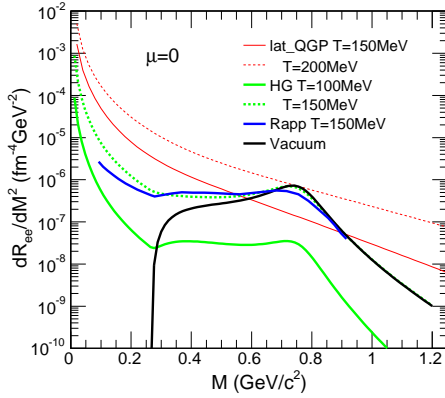


Figure 9: (Color Online) Emission rates of dielectrons from QGP phase (red thin lines) at temperature: 150 MeV (solid line), 200 MeV (dashed line), and HG phase (green thick lines) at temperature: 100 MeV (solid line), 150 MeV (dashed line). The vacuum contribution to HG rate at 150 MeV is shown as black dashed line. HG rate from effective interaction Lagrangians [26] at 150 MeV is shown as blue dashed-dotted line.

spectra and elliptic flow of dileptons in QGP phase and HG phase has been investigated [27]. Similar work has been done for direct photons [28]. The elliptic flow of dileptons seems more sensitive to viscous effect than their spectra, however, it remains a modest effect.

D. Elliptic flow v_2 and Triangular flow v_3

The elliptic flow v_2 and the triangular one v_3 of thermal photons/dileptons are calculated in a similar way as in Refs [4].

For each event, the azimuthal angle dependence of the transverse momentum spectrum of thermal direct pho-

tons or of the invariant mass spectrum of thermal dielectrons can be decomposed into harmonics of the azimuthal angle ϕ as

$$\frac{dN}{d\phi} \sim \frac{1}{2\pi} [1 + 2v_2 \cos 2(\phi - \psi_2) + 2v_3 \cos 3(\phi - \psi_3) + \dots], \quad (21)$$

where $v_2(v_n)$ is the elliptic flow (higher order harmonics), and ψ_n is the n th-order event plane angle. Obviously, v_n and ψ_n depend on the dielectron's invariant mass M and vary event by event. From Eq. (21), one can easily get

$$v_{e,n} \cos(n\psi_{e,n}) = \frac{\int_0^{2\pi} \cos(n\phi) \frac{dN}{d\phi} |_e d\phi}{\int_0^{2\pi} \frac{dN}{d\phi} |_e d\phi} \quad (22)$$

$$v_{e,n} \sin(n\psi_{e,n}) = \frac{\int_0^{2\pi} \sin(n\phi) \frac{dN}{d\phi} |_e d\phi}{\int_0^{2\pi} \frac{dN}{d\phi} |_e d\phi}, \quad (23)$$

with the subscript e added to emphasis variables for a single event. Let's note their right sides as $\langle \cos n\phi \rangle_e$ and $\langle \sin n\phi \rangle_e$, respectively. Then, for each event, the harmonics and reaction plane of order n can be obtained as

$$v_{e,n} = \sqrt{\langle \cos(n\phi) \rangle_e^2 + \langle \sin(n\phi) \rangle_e^2} \quad (24)$$

and

$$\psi_{e,n} = \frac{1}{n} \arctan \frac{\langle \sin(n\phi) \rangle_e}{\langle \cos(n\phi) \rangle_e}. \quad (25)$$

The elliptic flow v_2 and higher order harmonics v_n of the sample is obtained via event average

$$v_n = \sum_{e=1}^N \frac{v_{e,n}}{N}. \quad (26)$$

This is equivalent to the definition in [29].

To obtain the flow coefficients v_n of direct photons, the yield of prompt photons should be taken into the average. Vanishing coefficients v_n are assumed for prompt photons since collective motion has not yet involved at that time. Because prompt photons dominant at high transverse momentum p_t as seen in the following, the flow coefficients of direct photons vanish at high p_t .

III. RESULTS

First we check how well the hydrodynamic evolution is constrained by hadron data. EPOS3 made a reasonable reproduction of the rapidity distributions and transverse momentum spectra of not only charged hadrons but also identified particles. Here we show some relevant results. First the transverse momentum spectra of charged hadrons from AuAu collisions at 200 GeV , with different centrality, as shown in Fig. 10. The lines are from

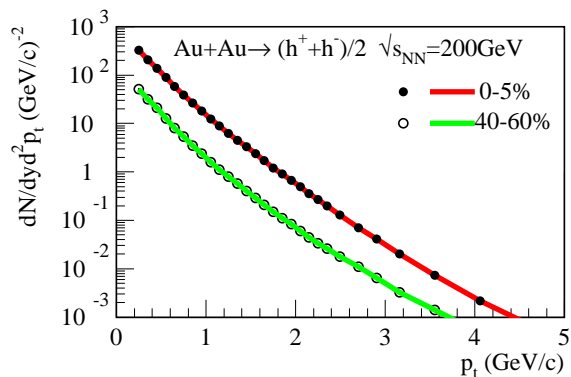


Figure 10: (Color Online) Transverse momentum spectra of charged hadrons from AuAu collisions at $\sqrt{s_{NN}} = 200$ GeV for centrality 0-5% and 40-60% simulated with EPOS3.102(lines). Data points from STAR [30].

EPOS3.102 simulation which coincide well with STAR data [30]. In Fig. 11 are shown the elliptic flow v_2 (left panels) and triangular flow v_3 (right panels) of charged hadron from AuAu collisions at 200 GeV with centrality 10-20% (upper panel) and 40-50% (lower panel). The different types of curves stand for different approaches to obtain hadrons flow, ie, cumulant approach with two particle pseudo-rapidity difference $\Delta\eta > 1$ (red solid lines), cumulant approach with $\Delta\eta > 2$ (green dashed lines), event plane approach (black thin dashed dotted lines), scalar product approach (blue thin dashed lines), participant plane approach (yellow dashed dotted lines). The coincidence to experimental data[31] (full dots) reveals a reasonable constraint to the anisotropy of the collision systems.

Then we show the photon results, from the spectra to flows. In Fig. 12, on the upper panels, the calculated transverse momentum spectra of direct photons (full solid lines) from AuAu collisions at three centrality classes, 0-20% (left panel), 20-40%(middle panel) and 40-60%(right panel), are decomposed to the two main sources, prompt (dotted lines) and thermal (dashed lines). The dominance of the two sources to the transverse momentum regions is clear shown. The total contribution are compared to the PHENIX data [32, 33]. This comparison is better shown in the lower panels. At high transverse momentum region, the prompt contribution is lower than data points constantly, for the centrality 0-20%. So the scaled binary collision number in this centrality is better doubled in this centrality. This shortcoming doesn't effect too much our judgement of the thermal emission, since the dominant p_t regions of the two sources are quite clear. At low transverse momentum region, the ratio Data/total is above unity, which means the thermal emission from our calculation is too low. The collision systems provided by EPOS3 do not shine enough, similar to the McGill results [5].

Now we present the anisotropic emission of photons. In Fig. 13, the elliptic flow v_2 (upper panels) and tri-

angular flow v_3 (lower panels) of photons (solid lines: direct photons) from AuAu collisions at 200GeV with centrality 0-20%, 20-40% and 40-60% (from left to right) are presented. The values of thermal photons are plotted as dashed lines. With the vanishing flows of prompt photons, the values of direct photons (red solid lines) are reduced, especially at high transverse momentum region. A good coincidence of the calculated elliptic flow to the PHENIX data[2] (Full dots) is obtained for the three centrality classes. For triangular flow, the coincidence between experimental data and theoretical results is less good and centrality dependent.

An interesting question is to know how does the elliptic flow and triangular flow of photons are built up with time. Here in Fig. 14 some snapshots of the yields (left panel) and elliptic flow v_2 (right panel) of thermal photons are shown. The increase of elliptic flow with time is evident. The elliptic flow at the initial time (red line) is zero because of the vanishment of the initial radial flow velocity. However, the yields of the initial time (also red line) is the largest, despite the smallest system size. High order coefficients v_n behave similar to v_2 . And so do the following thermal dileptons. The invariant mass effects not to the instantaneous flow coefficient, but to the instantaneous yields. And the observables comparable to the experimental measurements are time-integrated results.

Now we present the results of dileptons. First, in Fig. 15 are shown the contributions from different phases, QGP phase (red dotted lines) and HG phase (blue dashed lines), to the invariant mass spectrum (left panel) and the elliptic flow (right panel) of the midrapidity thermal dileptons from AuAu collisions at $\sqrt{s_{NN}} = 200$ GeV with centrality 10-40%. The QGP contribution dominates the thermal spectra at $M > 1$ GeV/ c^2 region, as in the above figure on emission rates. And the peak from the contribution of the hadronic phase indeed remains around the ρ mass after the space-time integral of the emission rate. The elliptic flow of HG phase, the latter phase, is larger, consistent with our above snapshots. The contributions of the two phases together make the green dashed dotted lines. Thus, in the total thermal spectrum, a pronounced peak still exists. The elliptic flow ranges between the upper bound (values in hadronic phase) and lower bound (values in QGP phase), and is close to the corresponding bound of the dominating phase. To compare with STAR data, we have to take into account of the detector acceptance factor due to single electron trigger as mentioned above. This acceptance efficiency factor reduces the thermal contribution over a large region of invariant mass M , particularly strongest at the small M , c.f. the solid line on the left panel. Its effect to the elliptic flow is ignorable for large M , but very strong at small M , c.f. the solid line in the right panel. In the following, this acceptance factor is always included in our results.

Next the invariant mass spectra is compared to STAR data. For the goal, non-thermal contribution such as STAR cocktail is included. STAR cocktail contribu-

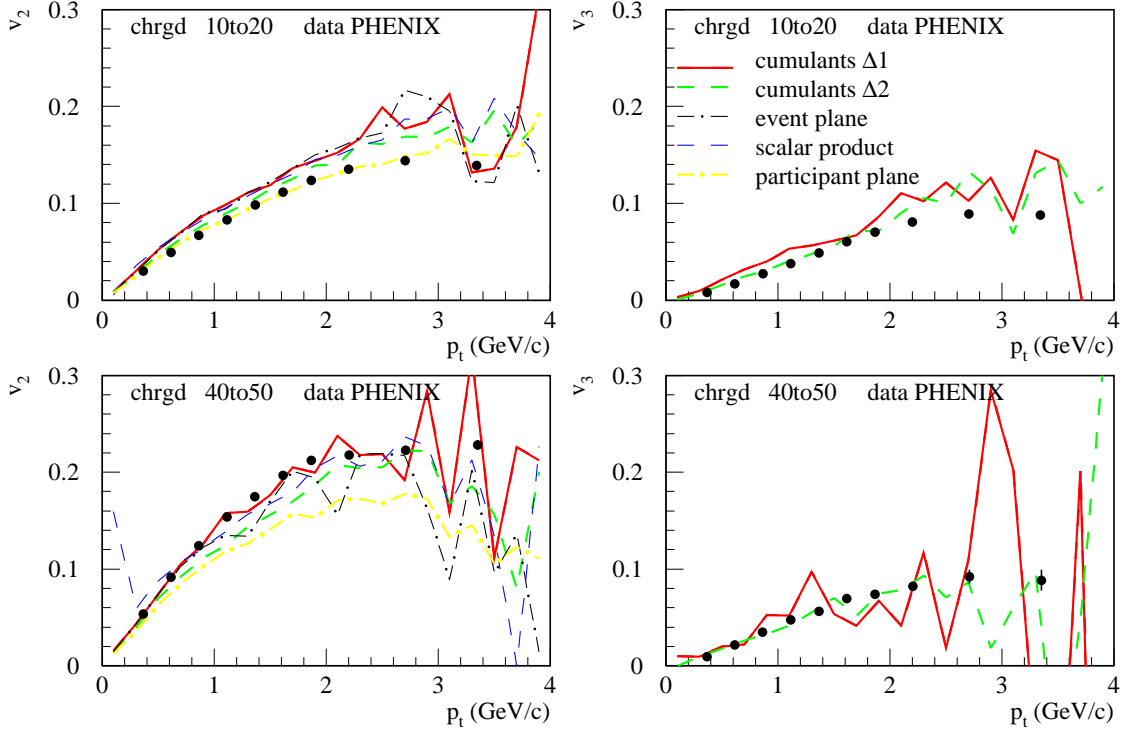


Figure 11: (Color Online) Elliptic flow v_2 (left panels) and triangular flow v_3 (right panels) of charged hadrons from AuAu collisions at $\sqrt{s_{NN}} = 200$ GeV for centrality 10-20% (left) and 40-50% (right). Data points from PHENIX [31].

tion includes all the non-thermal contributions, such as contributions from Drell-Yan process and decay of long lived hadrons, such as light mesons, D-mesons and so on. Based on the measurement of those hadrons, Tsallis fitting and decay simulation, provide us the invariant mass spectra of the cocktail contribution [35].

In Fig.16, the invariant mass spectrum of dielectron from 0-10% Au+Au central collisions at $\sqrt{s_{NN}} = 200$ GeV (solid line) is the sum of thermal contribution (dotted line) and the STAR cocktail (dashed line). At intermediate and high invariant mass region, it coincides with the STAR measured result (empty dots), because of the common cocktail contribution. At low invariant mass region, the calculated curve is lower than data points. More emission of thermal dilepton is needed to coincide with data, consistent to the photon results.

In Fig.17(left panel) the invariant mass spectra of dielectrons (thermal + cocktail) from Au+Au collisions at $\sqrt{s_{NN}} = 200$ GeV for different centralities are compared to STAR data [6, 36], from top to bottom: 0-10% (cen-

tral), 10-40%, 40-80% and 0-80% (MinBias). For better visibility, the latter three results are multiplied by factors: 0.05, 0.02 and 0.0002, respectively. In the right panel, the comparison is better shown as the ratio to the cocktail contribution. The calculated results are in fact lower than the data, for all centralities, similar to the previous results of thermal photons. We miss about a half of the thermal dileptons to coincide with data, for all centralities.

In Fig.18, the red solid line is our calculated elliptic flow of thermal di-electrons from Au+Au minimum bias collisions (0-80% centrality) at $\sqrt{s_{NN}} = 200$ GeV. (The dashed line is the result before taking into account of the acceptance factor of single electron trigger.) As a reference, we also show STAR data [37] (stars) of the elliptic flow of di-electrons (from all sources, of course). The calculated elliptic flow of thermal dielectrons is comparable, in fact even larger than data for all di-electrons. The cocktail contribution will inherit a certain elliptic flow because hadrons carry elliptic flow before decaying

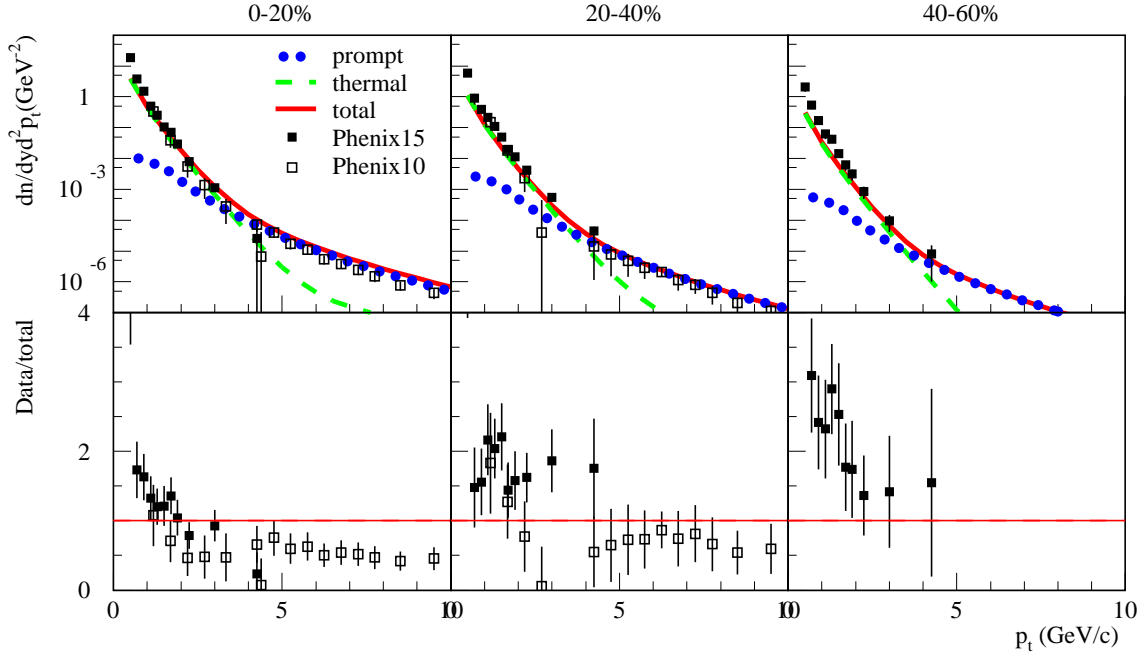


Figure 12: (Color Online) Upper panels: The transverse momentum spectra of photons from AuAu collisions at $\sqrt{s_{NN}} = 200$ GeV for centrality 0-20%, 20-40% and 40-60% (from left to right). Total direct photons (solid lines) are decomposed into two sources, prompt photons (dotted dashed lines) and thermal photons (dashed lines). Data points of direct photons from PHENIX [32, 33]. Lower panels: The ratio of PHENIX data to the calculated direct photons.

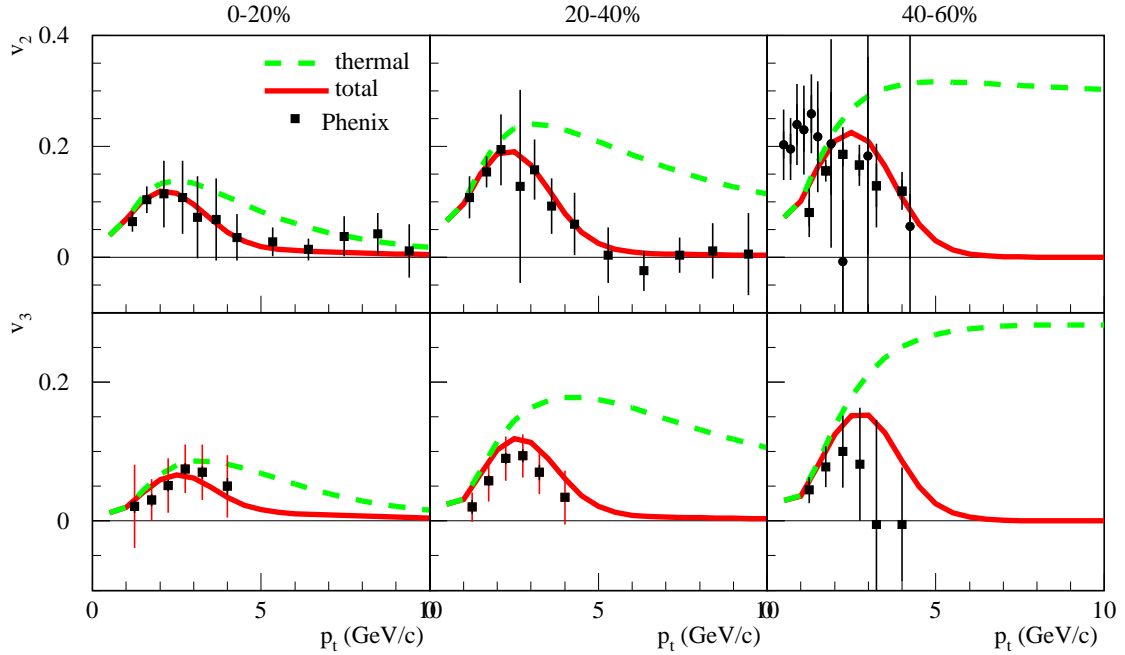


Figure 13: (Color Online) Elliptic flow v_2 (upper panels) and triangular flow v_3 (lower panels) of direct photons (solid lines) and thermal photons (dashed lines) from AuAu collisions at $\sqrt{s_{NN}} = 200$ GeV for centrality 0-20%, 20-40% and 40-60% (from left to right). Data points v_2 and v_3 of direct photons from PHENIX [34].

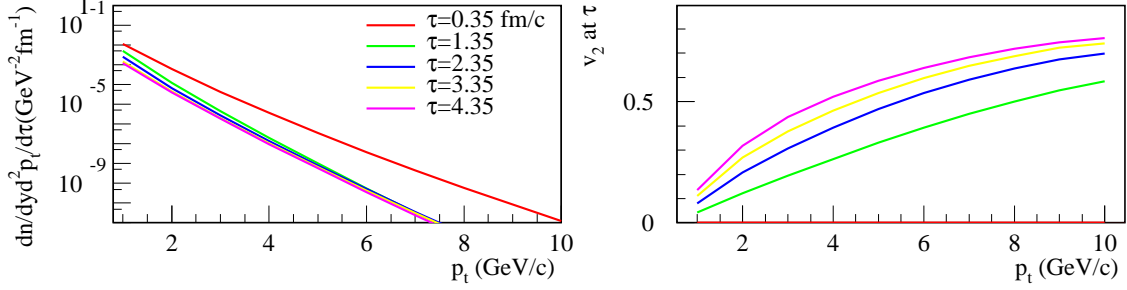


Figure 14: (Color Online) The snapshots of the yields (left panel) and elliptic flow v_2 (right panel) of thermal photons from AuAu collisions at $\sqrt{s_{NN}} = 200$ GeV for centrality 40-60%. Earlier emission makes more yield but smaller elliptic flow.

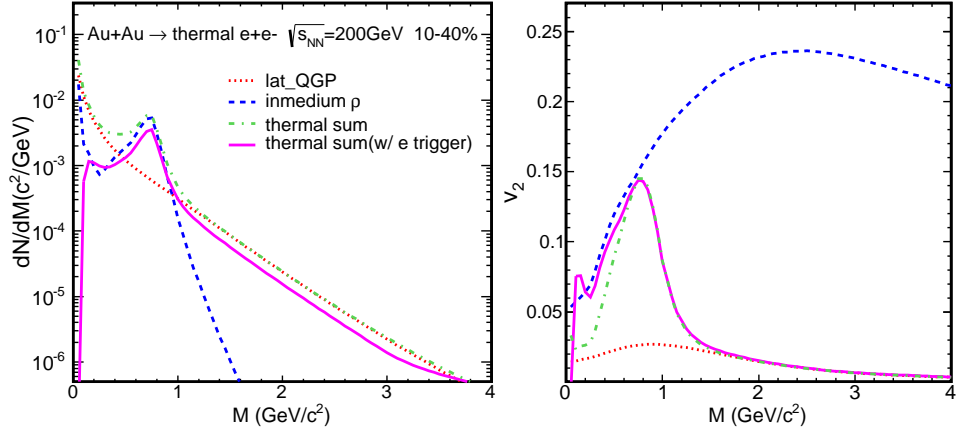


Figure 15: (Color Online) The invariant mass spectrum (left panel) and elliptic flow (right panel) of thermal di-electrons (green dotted dashed lines) from AuAu collisions at $\sqrt{s_{NN}} = 200$ GeV with centrality 10-40% are decomposed into di-electrons from QGP phase (red dotted lines) and hadronic phase (blue dashed lines). Solid lines are results with STAR single electron trigger. Following results without mention are all with this acceptance factor due to single electron trigger.

into di-electrons. Most models predict it to be lower than the STAR reference [19, 21, 38], whereas our result based on EPOS3 is larger.

To make a complete collection of our theoretical results, we present the centrality dependence and the n dependence of the flow harmonics v_n of dileptons in the following.

In Fig.19 is shown the elliptic flow of thermal dielectrons from AuAu collisions at $\sqrt{s_{NN}} = 200$ GeV for different centralities: 0-10% (pink dashed line), 10-40% (red dotted line), 40-80% (dark blue dashed-dotted line). The centrality dependence of high order n is also investigated. A strong centrality dependence, from central to peripheral collisions, occurs not only to the elliptic flow but also to higher order, $n = 3, 4, 5$.

In Fig.20, the higher order harmonics coefficients v_n ($n = 2, 3, 4, 5$) of thermal dielectrons from Au-Au collisions at $\sqrt{s_{NN}} = 200$ GeV with centrality of 10-40% is presented. The curves have same shape, same trend as direct photons. The magnitude decreases monotonically with the order n . And it is the case for all the investi-

gated centrality class, 0-10%, 10-40% and 40-80%. Such a behavior was observed for charged hadrons at low p_t by ALICE [39].

IV. DISCUSSION AND CONCLUSION

We investigated the anisotropic emission of photons and dileptons from Au+Au central collision at $\sqrt{s_{NN}} = 200$ GeV at the RHIC based on a hadron data constrained (3+1) dimensional hydrodynamic model EPOS3. All parameters are the default values of EPOS3.102 for the hydrodynamic evolution of the model. Thermal photons and dileptons are assumed to emit from hydro initial time, with the full rates introduced in the approach section, but without viscous correction in either QGP phase or HG phase.

The anisotropic emission of charged hadrons from the model agrees to experimental data at different centrality classes. And a good reproduction of the measured direct photon elliptic flow is obtained for all central-

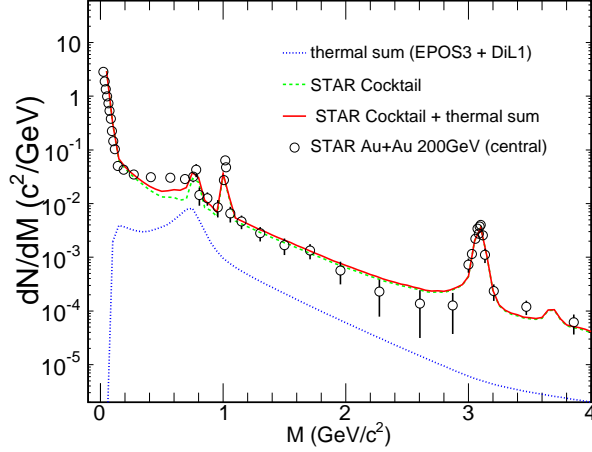


Figure 16: (Color Online) The invariant mass spectra of dielectrons from Au+Au collisions at $\sqrt{s_{NN}} = 200$ GeV for centrality 0-10% (solid line) is the sum of thermal contribution (dotted line) and STAR cocktail (dashed line). The measured invariant mass spectrum of dielectrons by STAR collaboration [6] are plotted as empty dots.

ities. Thus we predicted the elliptic flow of thermal dileptons, which is higher than the available results from other models, and comparable to the measured elliptic flow of total dileptons (thermal + cocktail) by STAR collaboration. We also made a prediction to high order flow coefficients of thermal dileptons, though our calcu-

lated triangular flow of direct photons does not coincide with PHENIX data so well. Since the triangular flow of charged hadrons calculated with cumulant approach agrees with data, and the deviation of triangular flow of direct photons from data has a centrality dependence, we should check whether the high order event planes of thermal emission defined in this way coincide with the experimental measurement in future. The event plane of second order defined so seems more reliable than those of higher order, due to the strong initial geometry.

The investigation of direct photons and dileptons from the same model, with a consistent description of the space-time evolution is useful. A underestimation of thermal photons from EPOS3.102 was found, compared with PHENIX measured transverse momentum spectra of direct photons. And a consistent underestimation of thermal dileptons was also found, compared with STAR measured invariant mass spectrum of dileptons. This shows a consistency between the two experimental measurements, and a requirement to improve the calculation for more thermal emissions.

Acknowledgments

S. X. Liu thanks J. Zhao and H. J. Xu for very helpful discussion. This work was supported by the Natural Science Foundation of China under Project No.11275081 and by the Program for New Century Excellent Talents in University (NCET).

-
- [1] E. Shuryak, Phys. Lett. B **78** (1978) 150.
 - [2] A. Adare *et al.* [PHENIX Collaboration], Phys. Rev. Lett. **109**, 122302 (2012) [arXiv:1105.4126 [nucl-ex]].
 - [3] A. Adare *et al.* (PHENIX Collaboration), Phys. Rev. C **81**, 034911 (2010).
 - [4] Fu-Ming Liu, and Sheng-Xu Liu, Phys. Rev. C **89** (2014) 034906.
 - [5] J. F. Paquet, C. Shen, G. S. Denicol, M. Luzum, B. Schenke, S. Jeon and C. Gale, Phys. Rev. C **93** (2016) no.4, 044906 doi:10.1103/PhysRevC.93.044906 [arXiv:1509.06738 [hep-ph]].
 - [6] L. Adamczyk *et al.* (STAR Collaboration), Phys. Rev. Lett. **113**, 022301 (2014).
 - [7] K. Werner, B. Guiot, Iu. Karpenko, T. Pierog, arXiv:1312.1233 [nucl-th]. Published in Phys. Rev. C **89** (2014) 6, 064903.
 - [8] H.J. Drescher, M. Hladik, S. Ostapchenko, T. Pierog, K. Werner, Phys.Rept. 350 (2001) 93-289.
 - [9] K. Werner, Iu. Karpenko, T. Pierog, M. Bleicher, K. Mikhailov, Phys.Rev. C **82** (2010) 044904.
 - [10] Klaus Werner, Phys.Rev.Lett. **98** (2007) 152301.
 - [11] M. Bleicher *et al.*, J. Phys. G **25** (1999) 1859; H. Petersen, J. Steinheimer, G. Burau, M. Bleicher and H. Stocker, Phys. Rev. C **78** (2008) 044901.
 - [12] P. Arnold, G. D. Moore, and L. G. Yaffe, J. High Energy Phys. **0111**, 057 (2001); J. High Energy Phys. **0112**, 9 (2001).
 - [13] S. Turbide, R. Rapp and C. Gale, Phys. Rev. C **69**, 014903 (2004) [hep-ph/0308085].
 - [14] S. S. Adler *et al.* [PHENIX Collaboration], Phys. Rev. Lett. **98** (2007) 012002 doi:10.1103/PhysRevLett.98.012002 [hep-ex/0609031].
 - [15] F. M. Liu and K. Werner, Phys. Rev. Lett. **106** (2011) 242301 doi:10.1103/PhysRevLett.106.242301 [arXiv:1102.1052 [hep-ph]].
 - [16] K.J. Eskola, V.J. Kolhinen and C.A. Salgado, Eur. Phys. J. C **9**, 61 (1999); K.J. Eskola, V.J. Kolhinen and P.V. Ruuskanen, Nucl. Phys. B **535**, 351 (1998).
 - [17] R. Rapp and J. Wambach, Adv. Nucl. Phys. **25** (2000) 1.
 - [18] H. T. Ding, A. Francis, O. Kaczmarek, F. Karsch, E. Laermann and W. Soeldner, Phys. Rev. D **83**, 034504 (2011).
 - [19] R. Rapp, Adv.High Energy Phys. **2013** (2013) 148253, arXiv:1304.2309.
 - [20] G. J. Gounaris and J. J. Sakurai, Phys. Rev. Lett. **21**, 244 (Jul 1968).
 - [21] G. Vujanovic, C. Young, B. Schenke, R. Rapp, S. J. Jeon and C. Gale, Phys. Rev. C **89** (2014) 034904.
 - [22] C. Gale and J. I. Kapusta, Nucl. Phys. **B357**, 65 (1991).
 - [23] R. F. Schwitters and K. Strauch, Annu. Rev. Nucl. Sci. **26**, 89 (1976).

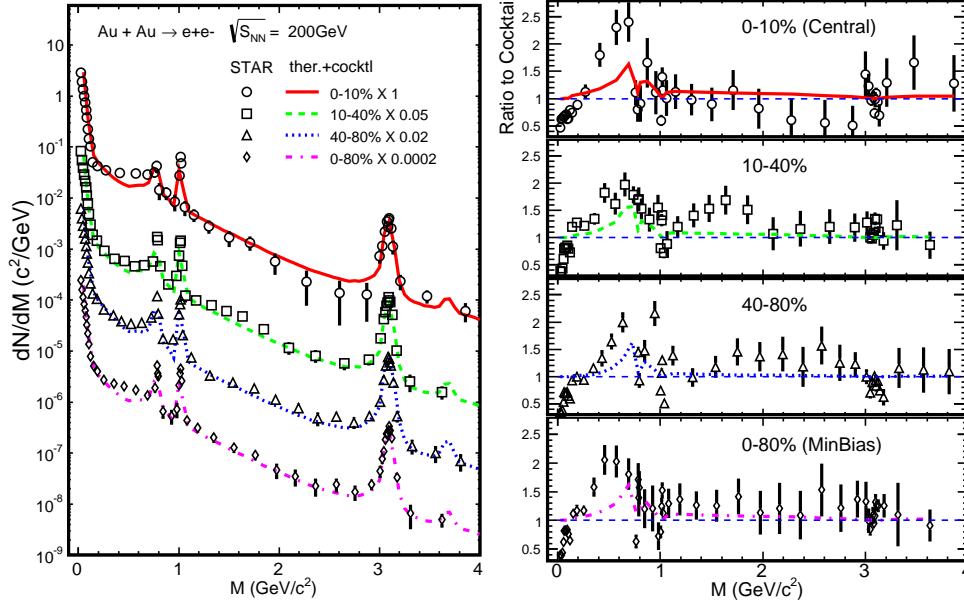


Figure 17: (Color Online) Left panel: The invariant mass spectra of dielectrons (thermal+cocktail) are compared to STAR data [6, 36], for four centrality classes, 0-10% (central), 10-40%, 40-80% and 0-80% (minimal bias) (from top to bottom). Right panel: The comparison is shown as the ratio to the cocktail contribution.

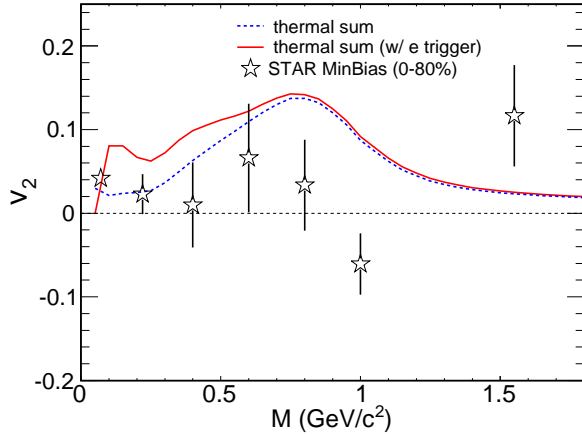


Figure 18: (Color Online) Thermal elliptic flow of dielectrons from $\sqrt{s_{NN}} = 200$ GeV Au+Au minimum bias collisions and comparison with STAR data [37].

- [24] Hao-jie Xu, Hong-fang Chen, Xin Dong, Qun Wang, and Yi-fei Zhang, Phys. Rev. C **85**, 024906 (2012).
 [25] V. L. Eletsky, M. Belkacem, P. J. Ellis, and J. I. Kapusta, Phys. Rev. C **64**, 035202 (2001).

- [26] R. Rapp, Phys. Rev. C **60**, 024903 (1999).
 [27] G. Vujanovic, C. Young, B. Schenke, S. Jeon, R. Rapp and C. Gale, Nucl. Phys. A **904-905**, 557c (2013) [arXiv:1211.0022 [hep-ph]].
 [28] C. Shen, U. W. Heinz, J. F. Paquet and C. Gale, Phys. Rev. C **89**, no. 4, 044910 (2014) [arXiv:1308.2440 [nucl-th]].
 [29] C. Gale, S. Jeon, B. Schenke, P. Tribedy and R. Venugopalan, Phys. Rev. Lett. **110**, no. 1, 012302 (2013) [arXiv:1209.6330 [nucl-th]].
 [30] J. Adams *et al.* [STAR Collaboration], Phys. Rev. Lett. **91**, 172302 (2003) doi:10.1103/PhysRevLett.91.172302 [nucl-ex/0305015].
 [31] A. Adare *et al.* [PHENIX Collaboration], Phys. Rev. Lett. **107**, 252301 (2011) doi:10.1103/PhysRevLett.107.252301 [arXiv:1105.3928 [nucl-ex]].
 [32] A. Adare *et al.* [PHENIX Collaboration], Phys. Rev. Lett. **104**, 132301 (2010) doi:10.1103/PhysRevLett.104.132301 [arXiv:0804.4168 [nucl-ex]].
 [33] A. Adare *et al.* [PHENIX Collaboration], Phys. Rev. C **91** (2015) no.6, 064904 [arXiv:1405.3940 [nucl-ex]].
 [34] B. Bannier [PHENIX Collaboration], Nucl. Phys. A **931**, 1189 (2014) doi:10.1016/j.nuclphysa.2014.08.034 [arXiv:1408.0466 [nucl-ex]].
 [35] L. Adamczyk *et al.* (STAR Collaboration) Phys. Rev. C **86** (2012) 024906.
 [36] L. Adamczyk *et al.* (STAR Collaboration) (2015) arXiv:1504.01317.

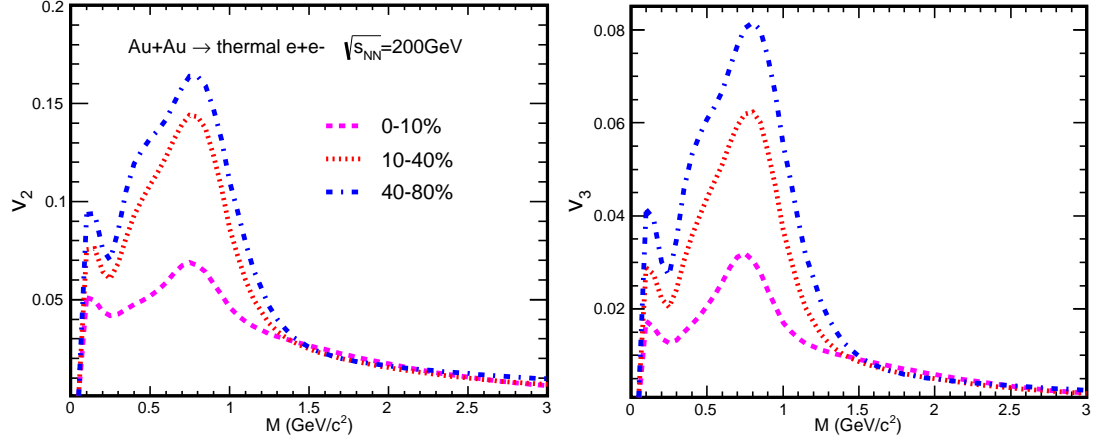


Figure 19: (Color Online) The elliptic flow (left) and triangler flow (right) of thermal dielectrons from AuAu collisions at $\sqrt{s_{NN}} = 200$ GeV. 0-10%(pink dashed line), 10-40%(red dotted line), 40-80%(dark blue dashed-dotted line).

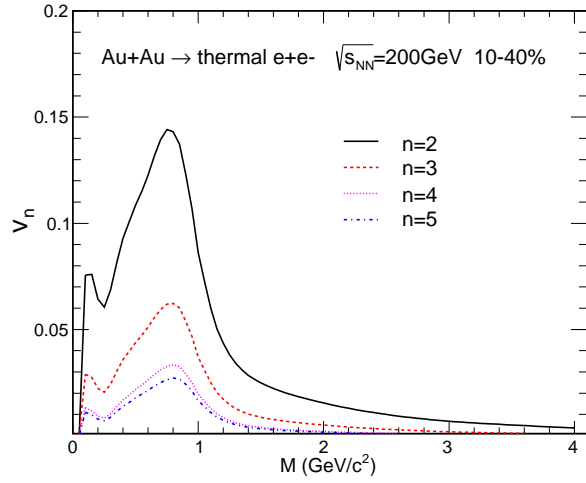


Figure 20: (Color Online) Predicated harmonics coefficients v_n ($n = 2, 3, 4, 5$) of thermal dielectrons are shown by various curves for centrality 10-40%.

- [37] L. Adamczyk *et al.* (STAR Collaboration) Phys. Rev. C **90** (2014) 64904.
- [38] Hao-Jie Xu, Longgang Pang, Qun Wang, Phys. Rev. C **89**(2014) 064902.
- [39] K. Aamodt *et al.* [ALICE Collaboration], Phys. Rev. Lett. **107**, 032301 (2011) [arXiv:1105.3865 [nucl-ex]].